Resistance-Spot-Welded AZ31 Magnesium Alloys: Part I. Dependence of Fusion Zone Microstructures on Second-Phase Particles

L. XIAO, L. LIU, Y. ZHOU, and S. ESMAEILI

A comparison of microstructural features in resistance spot welds of two AZ31 magnesium (Mg) alloys, AZ31-SA (from supplier A) and AZ31-SB (from supplier B), with the same sheet thickness and welding conditions, was performed *via* optical microscopy, scanning electron microscopy (SEM), X-ray diffraction (XRD), and transmission electron microscopy (TEM). These alloys have similar chemical composition but different sizes of second-phase particles due to manufacturing process differences. Both columnar and equiaxed dendritic structures were observed in the weld fusion zones of these AZ31 SA and SB alloys. However, columnar dendritic grains were well developed and the width of the columnar dendritic zone (CDZ) was much larger in the SB alloy. In contrast, columnar grains were restricted within narrow strip regions, and equiaxed grains were promoted in the SA alloy. Microstructural examination showed that the as-received Mg alloys contained two sizes of Al_8Mn_5 second-phase particles. Submicron Al_8Mn_5 particles of 0.09 to 0.4 μm in length occured in both SA and SB alloys; however, larger Al_8Mn_5 particles of 4 to 10 μm in length were observed only in the SA alloy. The welding process did not have a great effect on the populations of Al_8Mn_5 particles in these AZ31 welds. The earlier columnar-equiaxed transition (CET) is believed to be related to the pre-existence of the coarse Al_8Mn_5 intermetallic phases in the SA alloy as an inoculant of α-Mg heterogeneous nucleation. This was revealed by the presence of Al_8Mn_5 particles at the origin of some equiaxed dendrites. Finally, the columnar grains of the SB alloy, which did not contain coarse second-phase particles, were efficiently restrained and equiaxed grains were found to be promoted by adding 10 μm-long Mn particles into the fusion zone during resistance spot welding (RSW).

DOI: 10.1007/s11661-010-0197-3

I. INTRODUCTION

As one of the predominant joining techniques in sheet metal assembly, resistance spot welding (RSW) is a primary method for joining automotive structural components due to its advantages in terms of welding efficiency and automation. Magnesium (Mg) alloys have recently received strong research interest in the automobile industry, since considerable weight savings can be realized by substituting aluminum or steel components with these alloys. The behavior of Mg alloys during RSW is different from that of steel or Al alloys due to their lower melting point, greater fluidity, higher chemical activity, higher thermal and electrical conductivity, and larger coefficient of linear expansion. The differences in thermal, structural, and electrical properties also lead to differences in solidification microstructure of alloys.[1,2] It has been found that the strength of Mg alloy weldments is much lower than that of the base material and also that the weldability of Mg alloys joined by conventional fusion welding is inferior to that of steel.[1,2]

In fusion welds, columnar and equiaxed grains are often the predominant macrostructural constituents.[3–6] The columnar dendritic structure formed in the fusion zone can seriously compromise the mechanical properties of the joints. Equiaxed grain structure in welds usually is more desirable than columnar, since the former may have less segregation of alloying elements and, hence, more isotropic microstructure and mechanical properties. Moveover, fine equiaxed grains enhance mechanical properties as well. Therefore, there has been considerable experimental research on the columnar-equiaxed transition (CET) in welds, mainly of aluminum alloys and stainless steel, but not of Mg alloys.[7–11] Various grain refinement techniques have been applied in controlling the bead microstructures, such as electromagnetic stirring, current pulsing, torch vibration, arc oscillation, and inoculation.[6,12] Among them, inoculation using grain refining agents offers the greatest promise for practical application.[13–16] In aluminum gas-tungsten arc (GTA) welds, Kerr and co-workers[7,8] and later Kou and Le[10,11] observed that Ti-rich particles acting as heterogeneous nucleation sites promoted CET.

The presence of sufficient nucleants, a low thermal gradient, and a high solid/liquid interface velocity

L. XIAO and L. LIU, Ph.D. Candidates, Y. ZHOU, Professor, and S. ESMAEILI, Assistant Professor, are with the Department of Mechanical & Mechatronics Engineering, University of Waterloo, Waterloo, ON, Canada N2L 3G1. Contact e-mail: nzhou@mecheng1.uwaterloo.ca L. LIU is also a Ph.D. Candidate with the State Key Laboratory of Advanced Welding Production Technology, Harbin Institute of Technology, Harbin, P.R. China.

Manuscript submitted April 14, 2009.
Article published online March 27, 2010

usually favors the CET.[6–16] Several mechanisms have been proposed to assist the CET during solidification of welds, including surface nucleation,[9,17] dendrite fragmentation,[6,9,12] grain detachment,[6,8] and heterogeneous nucleation.[6–16] It is commonly accepted that the ratio of G_L/R is an appropriate parameter to predict the CET,[4,7,9,11] where G_L is thermal gradient and R is solidification rate. A low G_L/R value implies a larger constitutionally undercooled zone ahead of the columnar grain front and an enhanced nucleation of equiaxed grains.[4,7,9,11] Hallum and Baeslack[18] inoculated titanium alloy GTA welds with Ti-6Al-4V powder and observed that the powder additions reduced the melt temperature and lowered the thermal gradients near the tail of the weld pool, thus favoring equiaxed grain growth by heterogeneous nucleation on partially melted powder particles. Kato *et al.*[19] showed that increasing the alloying element content favors a CET, because they contribute to the development of constitutional undercooling depending on their growth restriction effect. Although the CET has been succssfully promoted in welds by adjusting the welding process or introducing foreign inoculants, the precise mechanism is often not fully understood.

It has long been realized that the microstructure of Mg-Al alloys depends on the presence of impurity elements and second-phase particles. Earlier work by Tiner[20] showed that Mg-Al alloys containing 0.19 pct Mn or more (up to 0.98 pct Mn) demonstrated grain refinement. More recently, Byun *et al.*[21] investigated the effect of different Mn addition levels on the microstructure of the AZ91 alloy and suggested that $Al_8(Mn,Fe)_5$ particles acted as effective nucleation sites.[21] Grain refinement was achieved in a commercial AZ31 alloy by an addition of Mn in the form of an Al-60 pct Mn master alloy, due to the presence of hexagonal-close-packed (hcp) ε-AlMn phase particles that could act as nucleants for α-Mg grains.[15] Using the edge-to-edge matching model, Qiu *et al.*[16] compared the grain refining efficiency of various (Al, Mn)-containing phases that exist in Mg-Al alloys. The results show that a metastable τ-AlMn phase possesses significantly better crystallographic matching to α-Mg matrix than the other Al-Mn intermetallic phases and could therefore serve as an effective heterogenous nucleation site. However, further convincing experimental evidence is needed to prove that the high-temperature ε-AlMn phase can be retained in the Mg alloys at low solidification temperatures. Laser *et al.*[22] also reported grain refinement by Al_8Mn_5 particles in AZ31 alloys even though Al_8Mn_5 has a rather high atomic mismatch energy against α-Mg. As atomic mismatch limits the effectiveness of particles as heterogeneous nucleation sites, some researchers tend to believe that one or more Al-Mn or Al-Mn-Fe intermetallic compounds may form at high temperature and act as effective grain refiners during subsequent cooling of Mg-Al alloy.[21–23]

Although grain refinement of Mg alloy castings using inoculants containing Mn and Al has been investigated,[15,16,20–23] less attention has been paid to the microstructural improvement of Mg alloy welds. On the other hand, the CET has been studied in GTA welding of Al and steels,[7–11] but not in resistance welding. Therefore, it is important to characterize the microstructures of RSW in Mg alloys[24,25] and understand their dependence on second-phase particles across Mg alloy welds.

We received two groups of AZ31 Mg alloy sheets, which have a similar chemical composition but different sizes of second-phase particles due to different manufacturing processes used by different suppliers. The objective of this work is to study the dependence of microstructure on second-phase particles in RSW of AZ31 Mg alloys and ascertain an effective method to promote CET in these alloys.

II. EXPERIMENTAL PROCEDURES

The materials used in this work were two commercial grade hot-rolled sheets of AZ31 (SA from supplier A and SB from supplier B) Mg alloys supplied by different companies, where they were produced through independent processes. The chemical compositions of these alloys were analyzed using an inductively coupled plasma-atom emission spectrometer and mass spectrometer. As Table I shows, excepting some difference in Zn concentration, the alloys have similar chemical composition.

Rectangular welding specimens of 100 mm × 25 mm × 1.5 mm were cut parallel to the rolling direction of the sheets. The alloy SA sheets were mechanically ground from 2 to 1.5 mm in thickness, which is the thickness of the SB alloy. Then, both alloy samples were mechanically ground using 600 mesh abrasive paper in order to minimize the effect of surface roughness of samples on welding behavior. Furthermore, the surfaces of the plates were chemically cleaned, using a solution of 2.5 g chromic oxide and 100 mL distilled water before welding, as suggested by previous work.[26] Welding was performed by the conventional RSW technique using a S-400 Robotron 600V single-phase AC spot welding machine (Centreline (Windsor) Ltd., Windsor, ON, Canada). The welding conditions are listed in Table II. Six welding samples were welded under each welding condition: three for the tensile-shear test and three for the examination of microstructure. Furthermore, a variety of welding currents, hold times, and electrode forces were tested. The effect of welding current and hold time on mechanical properties and microstructures

Table I. Chemical Composition of Two AZ31 Alloys (Weight Percent)

Alloys	Al	Zn	Mn	Si	Zr	Ca	RE	Mg
SA	2.92	1.09	0.3	0.01	<0.01	<0.01	<0.01	bal
SB	3.02	0.80	0.3	0.01	<0.01	<0.01	<0.01	bal

Table II. Welding Parameters Selected in This Work

Welding Current (kA)	Electrode Force (kN)	Welding Time (Cycles)	Squeezing Time (Cycles)	Cooling Time (Cycles)
26	4	8	30	30

of AZ31 Mg alloy welds will be described in a companion article.[27]

Following RSW, all specimens for metallographic and scanning electron microscopy (SEM) examinations were cut, cold-mounted, ground, mechanically polished, and then chemically polished for 5 seconds in 10 pct nital followed by etching for 5 seconds with a solution of 4.2 g picric acid, 10 mL acetic acid, 70 mL ethanol, and 10 mL water. The microstructures of the as-received and welded specimens were examined by optical microscope, a JEOL* JSM-6460 scanning electron microscope equipped with an Oxford ultra-thin window detector energy-dispersive spectrometer (EDS, Oxford Instruments Microanalysis Group High Wycombe, Bucks, United Kingdom). X-ray microanalysis was performed in a Rigaku AFC-8 diffractometer with Cu target, 50 kV acceleration voltage, and 40 mA current (Rigaku Corporation, Tokyo, Japan).

*JEOL is a Japan Electron Optics Ltd., Tokyo.

For transmission electron microscopy (TEM), samples were cut on the base material and the cross section of welds using an electrical-discharge machine. Mechanical thinning of discs was continued to a thickness of 100 μm. The TEM foils were electropolished in a Tenupol 5 (Struers, Ballerup, Denmark) double jet polishing unit in a LiCl + Mg perchlorate + methanol + buthyloxyethanol solution at –45 °C. In the final step of sample preparation, the foils were subjected to short ion milling on a Fischione 1010 low-angle milling and polishing system in order to remove the surface oxide layer (Fischione Instruments, Inc., Murrysville, PA). The TEM investigations were performed with a PHILIPS** CM 200 electron microscope equipped with an Oxford ultrathin window detector EDS.

**PHILIPS is a trademark of Philips Electronic Instruments Corp., Mahwah, NJ.

III. RESULTS

A. *Microstructural Characterization across Weld Zones*

The optical microstructure was found to be comprised of equiaxed grains in the as-received AZ31 Mg alloys, as shown in Figures 1(a) and (b). The average grain size obtained by the linear intercept method was 8.4 μm for SA alloy and 7.5 μm for SB. Some strips of fine grain, distributed along the hot-rolled direction, were observed in both alloys. No obvious differences in microstructure were observed *via* optical microscope between SA and SB alloys in the as-received condition.

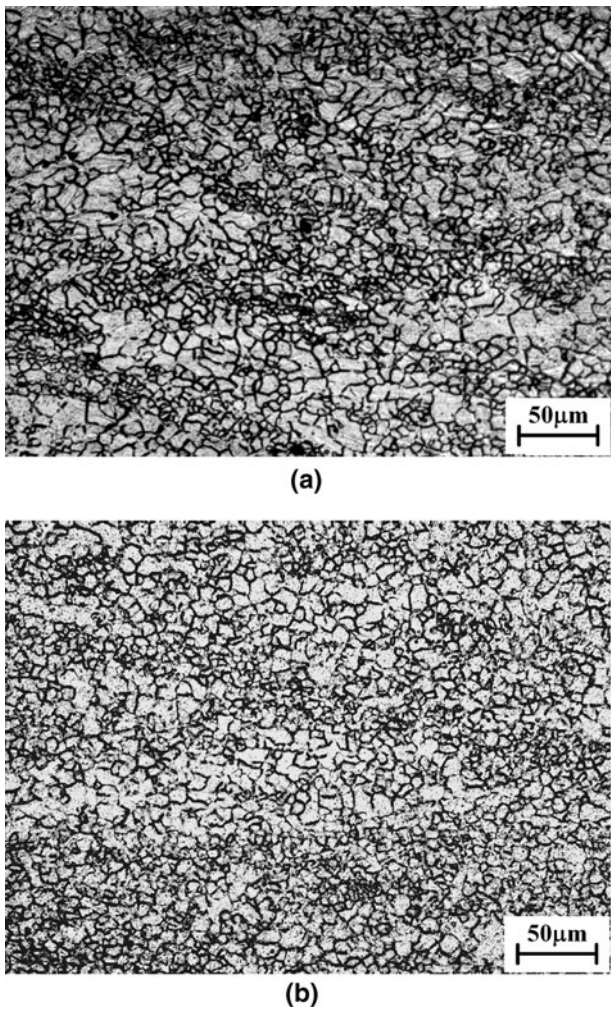

Fig. 1—Optical microstructure of two as-received AZ31 alloys in cross section: (*a*) SA alloy and (*b*) SB alloy.

Macrostructures of nuggets of two AZ31 alloy welds in the cross section are shown in Figures 2(a) and (b). The average nugget size is 7.30 mm × 1.84 mm (±0.05) for the SA alloy, similar to 7.36 mm × 1.94 mm (±0.05) for the SB alloy. Metallographic examinations were performed to identify microstructural features across the resistance welds in each alloy. A variety of structures were observed across the welds, as shown in Figures 3(a) and (b). Each weldment could be roughly divided into four zones with different microstructural features: base metal (BM), heat affected zone (HAZ), columnar dendritic zone (CDZ), and equiaxed dendritic zone (EDZ) in the fusion zone. The main difference in

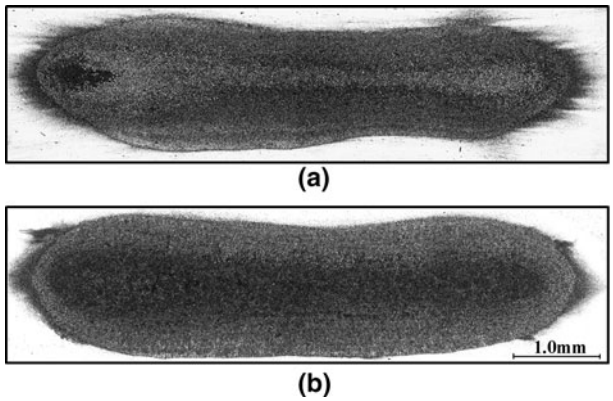

Fig. 2—Macrostructures of nuggets of two AZ31 alloy welds in the cross section: (*a*) SA alloy and (*b*) SB alloy.

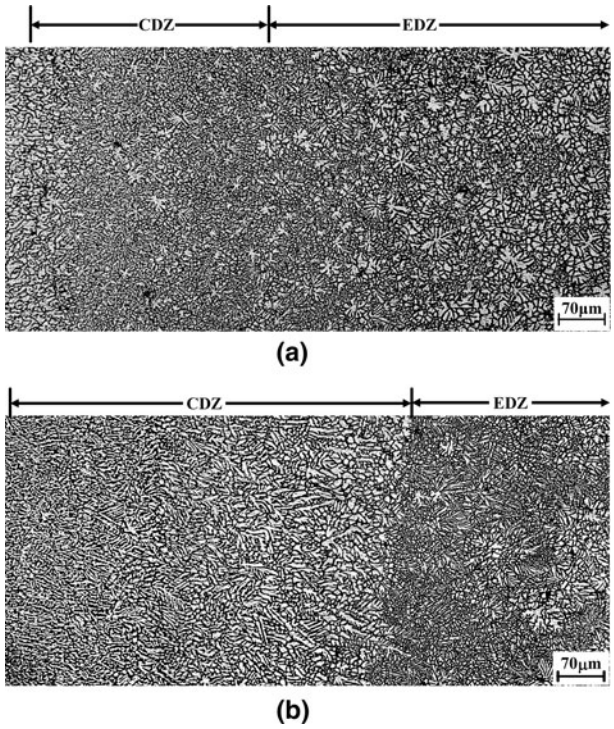

Fig. 3—Microstructure variation across RSW AZ31 alloy welds: (*a*) SA alloy and (*b*) SB alloy.

solidification microstructures between welds in the two alloys was in the size of the CDZ in the vicinity of the fusion boundary, as shown in Figures 4(a) and (b), respectively. In the SA alloy, columnar structure was restricted to a narrow strip region of 400 μm in width, and the ratio of length over width of columnar dendritic grains was small (Figure 4(a)). In contrast, well-developed columnar dendritic grains perpendicular to the fusion boundary within a band of 600 μm were produced in the SB alloy (Figure 4(b)). This indicates a much earlier CET in the SA alloy. As the solidification progressed toward the center of the nugget, equiaxed dendritic structure occurred in both SA and SB alloys, as shown in Figures 5(a) and (b). On a close examination, the diameter of the flowerlike dendritic structure in

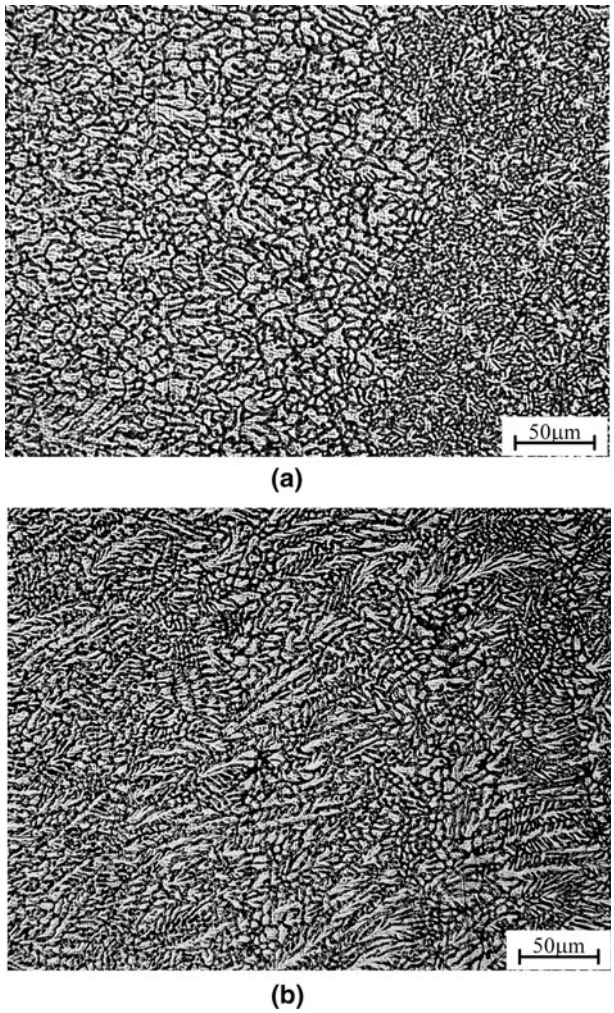

Fig. 4—CDZ formed in two AZ31 alloys: (*a*) undeveloped columnar dendritic structure in the SA alloy and (*b*) well-developed columnar dendritic structure in the SB alloy.

the SA alloy (Figure 5(a)) was found to be smaller than that in the SB alloy (Figure 5(b)). The average diameter of the flowerlike dendrites was about 55 μm in alloy SA and 85 μm in alloy SB.

B. *Microscopic Analysis of Second-Phase Particles*

1. *As-received AZ31 alloys*

SEM examination showed that the microstructure in the as-received SA and SB alloys was relatively homogeneous and consisted of an α-Mg matrix together with a large number of submicron white particles, as shown in Figures 6(a) and (b). These white particles were determined later by TEM to be β-$Mg_{17}Al_{12}$. Also, some rectangular and triangular second-phase particles of 4 to 10 μm in length were observed in the SA alloy, as indicated by an arrow in Figure 6(a). The volume fraction of these large particles in the SA alloy was estimated using a polished planar cross-sectional specimen by the manual point count procedure according to standard ASTM E562-05. It was about 0.15 pct. In contrast, second-phase particles of such size were not

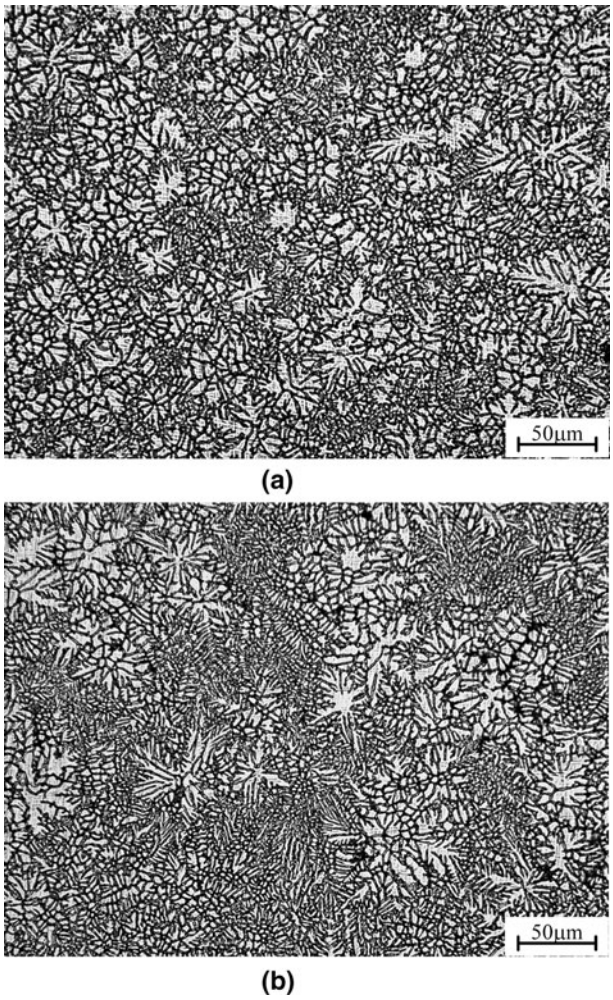

Fig. 5—EDZ formed in AZ31 alloys: (*a*) SA alloy and (*b*) SB alloy.

observed in the as-received SB alloy. Analysis of the large second-phase particles in SA alloy using EDS gave a result of 56.5 at. pct Al and 43.5 at. pct Mn, as shown in Figure 6(c). Some tiny peaks originating from Au were ignored. Considering the binary phase diagram of Al-Mn,[28] a Mn content between 20 and 27 at. pct corresponds to $Al_{11}Mn_4$, a Mn content between 37 and 50 at. pct corresponds to Al_8Mn_5, and a Mn content above 68 at. pct corresponds to β-Mn. These results suggest that the large particles in Figure 6(a) were primarily Al_8Mn_5.

Further examination revealed that the AZ31 microstructure of SA alloy in the as-received condition was composed of hcp α-Mg and submicron-sized body-centered-cubic β-phase $Mg_{17}(Al, Zn)_{12}$ precipitates, which were identified by a set of TEM selected area electron diffraction (SAED) patterns, as shown in Figure 7. The shape of the $Mg_{17}(Al, Zn)_{12}$ precipitates was ellipsoidal. When the incident electron beam was parallel to the $[01\bar{1}0]$ zone axis of the Mg matrix, the long axes of the ellipsoidal $Mg_{17}(Al, Zn)_{12}$ precipitates were parallel to the $[2\bar{1}\bar{1}0]$, [0002], and $[2\bar{1}\bar{1}2]$, respectively (Figure 7). The aspect ratio of long and short axes determined using TEM was up to about 5:1, and their maximum length was around 0.12 μm.

A large number of submicron Mn-Al second-phase paticles were also observed in both as-received SA and SB alloys. Figures 8(a) through (d) show typical bright-field (BF) and dark-field (DF) TEM images of the Al-Mn particles, and the selected area diffraction pattern (SADP) of a thin foil with $[01\bar{1}0]$ zone axis of the Mg matrix in the as-received SA alloy. Some of the second-phase particles gathered as a group, as shown in Figure 8(a). The secondary diffraction spots in the SADP in Figures 8(c) and (d) were found to be due to the presence of Al-Mn particles. The TEM dark-field image in Figure 8(b), which was obtained from the $(\bar{1}10)$ reflection presented in Figures 8(c) and (d), shows the submicron Al-Mn particle, also indicated by an arrow in Figure 8(a). The analysis of SADP showed that these submicron particles were Al_8Mn_5 with a size of 0.130-μm single particle and 0.4 μm in a group of particles when the zone axis of the Mg matrix is parallel to the $[01\bar{1}0]$. Furthermore, analysis of the second-phase particles using EDS indicated that primary constituent elements were Al and Mn, which is consistent with the results obtained with SEM, as shown in Figure 8(e). This spectrum was obtained in TEM mode with a nominal probe size of 0.15 ± 0.01 μm in diameter, which is larger than the diameter of the second-phase particles. Therefore, the peak of Mg together with some peaks of Ni and Zn in the spectrum in Figure 8(e) could be attributed to the contribution from α-Mg matrix. Some tiny Au peaks were ignored. Therefore, these TEM results demonstrated that the second-phase particles produced in the as-received SA alloy are Al_8Mn_5.

The same examination was performed on SB alloy in the as-received condition. The typical submicron Al_8Mn_5 particles are displayed in Figure 9. The diameter of these particles was around 0.09 μm in the form of single particle, and 0.2 μm in groups, which is slightly smaller than those formed in the SA alloy.

In summary, submicron Al_8Mn_5 second-phase particles of 0.09 to 0.4 μm in length were observed to form in both SA and SB alloys in the as-received condition. However, coarse Al_8Mn_5 particles of 4 to 10 μm in length were produced only in the as-received SA alloy.

2. *Fusion Zone*

Figures 10(a) through (c) show the SEM microstructures of second-phase particles in the welded SA alloy in HAZ, CDZ, and EDZ regions, respectively. The EDS analysis results are listed in Table III. Coarse second-phase particles of 4 to 10 μm in length were detected in each zone, as shown in Figures 10(a) through (c). A comparison of energy dispersive X-ray spectra recorded from the HAZ, CDZ, and EDZ in the welded SA alloy in Table III indicated that the composition of particles was between 35 and 48 at. pct for Mn and 45 and 55 at. pct for Al, which is similar to those obtained in the as-received SA alloy, in all three zones. This implies that there was not a large effect of welding process on the existence of Al_8Mn_5 intermetallic compounds in the SA alloy. The same SEM

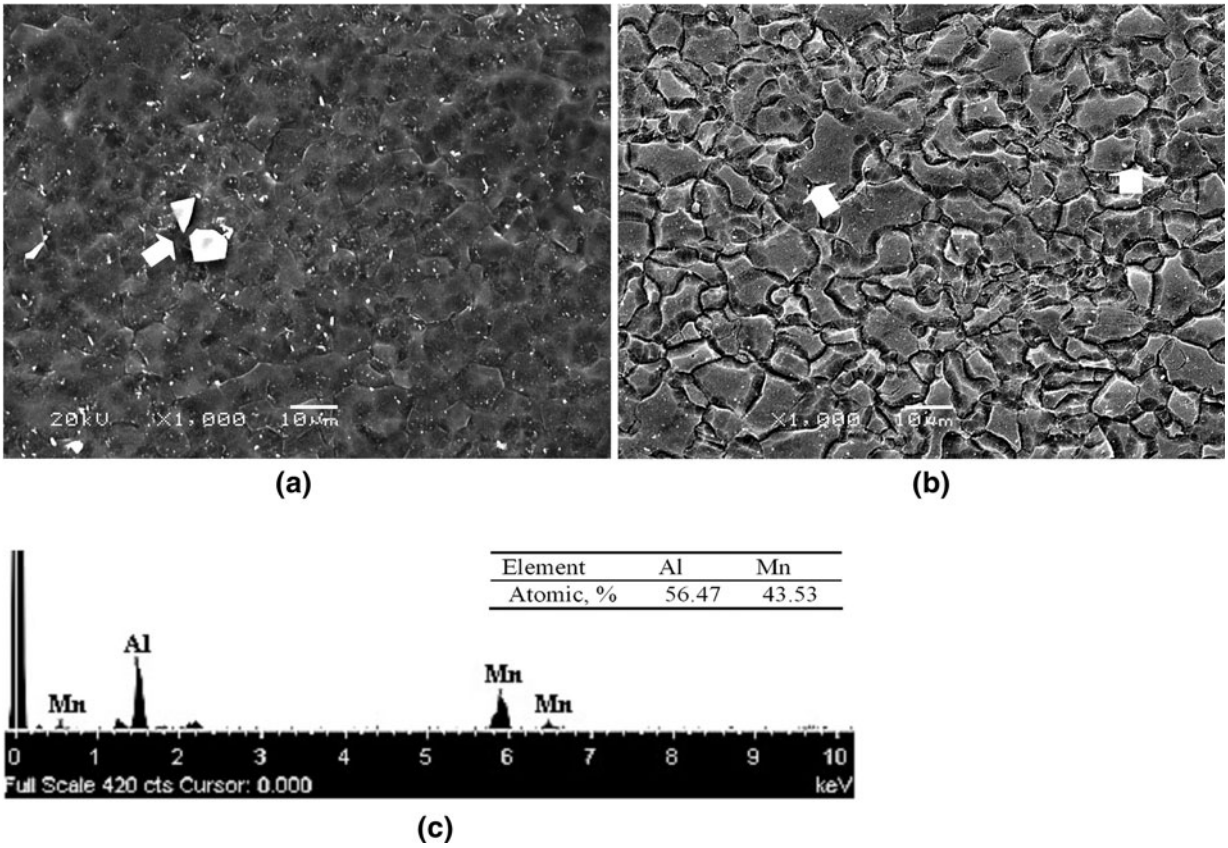

Fig. 6—SEM images of the as-received AZ31 SA and SB alloys and EDS analysis of the Al-Mn particles: (*a*) coarse Al-Mn particles, as indicated by an arrow in the SA alloy; (*b*) only tiny eutectic β-$Mg_{17}Al_{12}$ particles, as indicated by arrows in the SB alloy; and (*c*) EDS analysis of Al-Mn particles in the SA alloy.

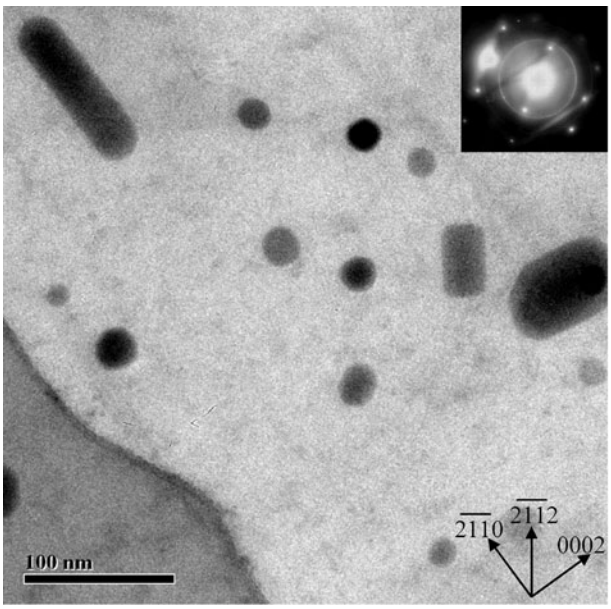

Fig. 7—TEM image of $Mg_{17}Al_{12}$ precipitates in the as-received SA alloy, incident beam || [01$\bar{1}$0].

examination was carried out on the SB alloy welds, and no such coarse (*i.e.*, 4 to 10 μm) Al-Mn particles were observed in the welded SB specimens.

Figures 11(a) through (d) show TEM images and SADP analysis of small particles observed in alloy SA welds. BF (Figure 11(a)) and DF (Figure 11(b)) images, and the corresponding SADP (Figures 11(c) and (d)), showed that these particles were Al_8Mn_5 intermetallic compound with a size of about 0.3 μm. Similar sized second-phase particles were observed in the welded SB alloy, as shown in Figures 12(a) and (b). From EDS analysis, ~35 at. pct Mn and ~65 at. pct Al were determined in the particles, indicating that they were also Al_8Mn_5.

In brief, two scales of particles were observed in the two AZ31 Mg alloys in the as-received and welded conditions. Micron-sized Al_8Mn_5 particles of 4 to 10 μm in length were only observed in the as-received and welded SA alloy. Submicron Al_8Mn_5 second-phase particles of 0.09 to 0.4 μm in length were detected in both SA and SB alloys in the as-received and welded conditions. The welding process did not have a great effect on the existence and size of Al_8Mn_5 second-phase particles in both SA and SB alloys.

C. *XRD Examination of Two AZ31 Alloys in the As-Received and Welded Conditions*

Phases formed in the as-received AZ31 SA and SB alloys were identified by X-ray diffraction (XRD) analysis, as shown in Figure 13(a). Peaks of α-Mg,

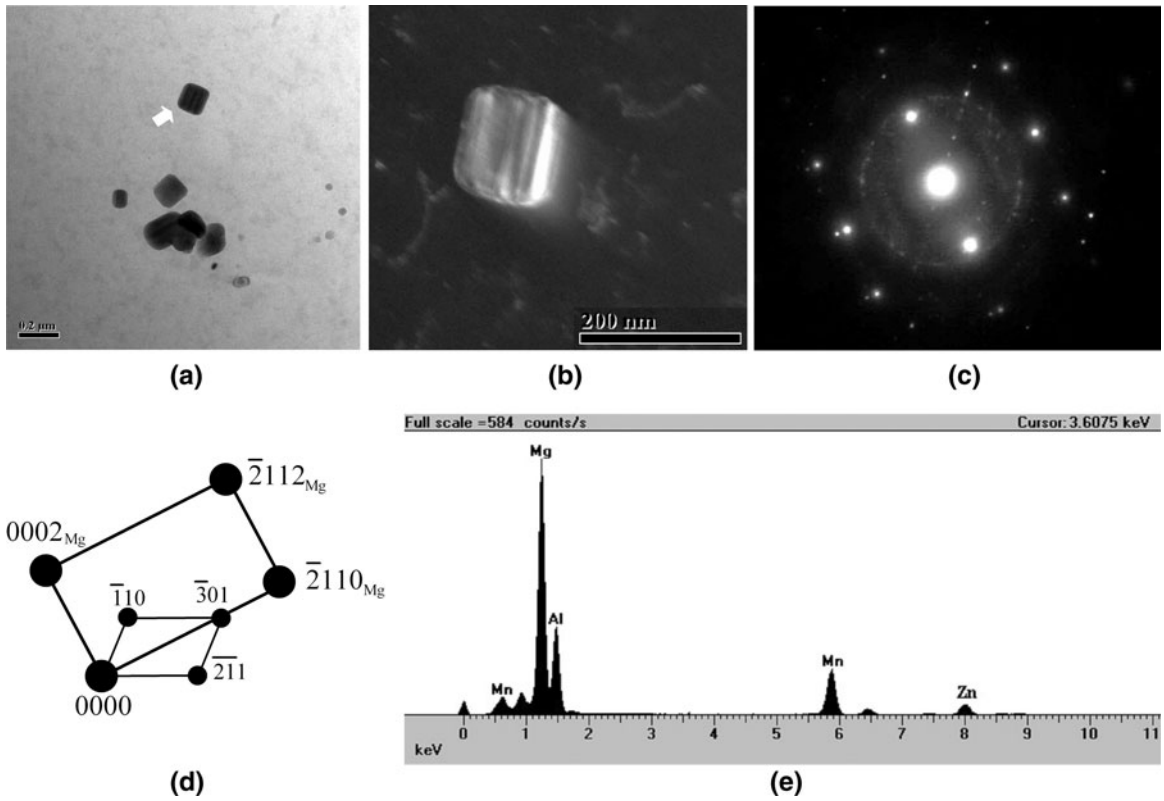

Fig. 8—TEM image, SAD, and EDS analysis of the Al-Mn particles formed in the as-received SA alloy: (*a*) bright field, (*b*) dark field, (*c*) SADP, (*d*) its schematic representation in the $[01\bar{1}0]_{Mg}$ zone axis, and (*e*) EDS.

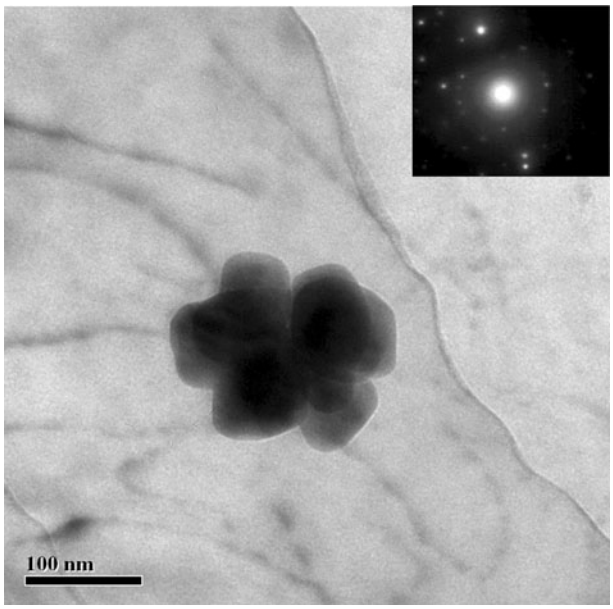

Fig. 9—TEM image of Al-Mn particles formed in the as-received SB alloy.

β-$Al_{12}Mg_{17}$, and Al_8Mn_5 were formed in the as-received SA and SB specimens. Further analysis demonstrated that the α-Mg produced the most intense peaks. Well-defined Al_8Mn_5 reflections were displayed, as well.

Figure 13(b) shows the XRD spectra of the two welded AZ31 alloys in the fusion zones. The results of XRD analysis showed that, besides Mg solid solution, β-$Mg_{17}Al_{12}$ and Al_8Mn_5 intermetallic compounds appeared in the fusion zone. These results have also confirmed the existence of Al_8Mn_5 intermetallic compounds in the welded SA and SB alloy specimens. In comparison with the as-received AZ31 alloys, the reflection peaks of the Al_8Mn_5 declined in the fusion zones in both alloys. In addition, some $Mg_{17}Al_{12}$ peaks were also identified by XRD in the fusion zones, as shown in Figure 13(b).

IV. DISCUSSION

A. *Mn-Al Particles in AZ31 Alloys*

Based on the theoretical calculations and experimental examinations, Laser *et al.*[22,29] suggested that some Al-Mn particles in the form of Al_8Mn_5 could be present on the dendritic boundaries and in the matrix in as-cast AZ31 alloy. By means of extraction technology, Liu *et al.*[30] observed that manganese existed in the as-cast AZ31 Mg alloys in the form of Al_8Mn_5 phases of 15- to 100-μm length or dissociated manganese particles. The rolling or extrusion process would not result in decomposition of Al_8Mn_5 phases, but could break them into finer spherical fragments with a size of about 4 to 5 μm.

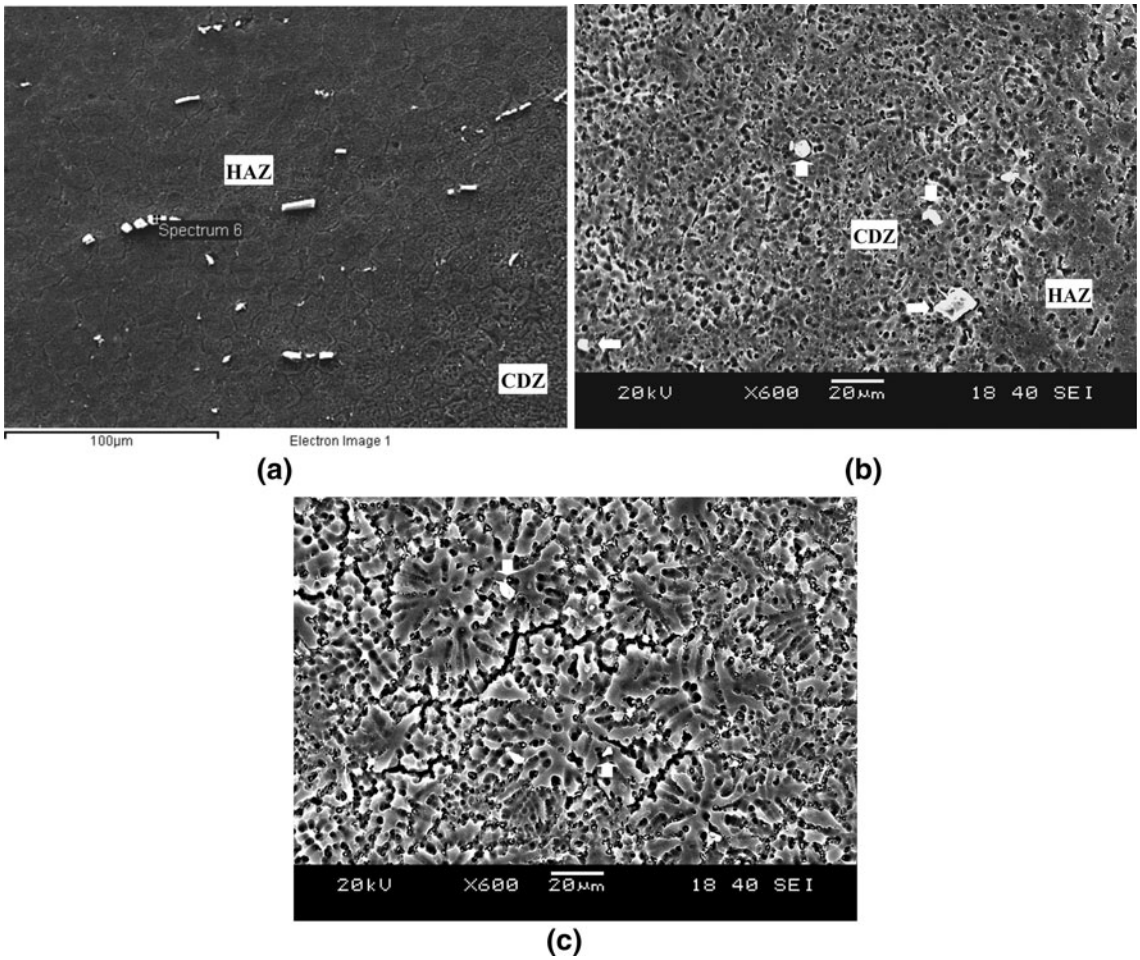

Fig. 10—SEM image of Al-Mn particles formed in the RSW welded SA alloy at different zones: (*a*) HAZ, (*b*) CDZ, and (*c*) EDZ.

Table III. EDS Analysis Results of Al-Mn Particles Formed in the RSW Weld SA Alloy at Different Zones

Element	HAZ	Atomic Percent CDZ	EDZ
Mg, K_α	19.65	—	6.81
Al, K_α	45.07	52.87	48.80
Mn, K_α	35.28	47.13	44.38

Al_8Mn_5 particles were observed to be present in AZ31 alloys in the as-received and welded conditions *via* SEM and TEM in this work. The welding process did not have a large effect on the existence of Al_8Mn_5 particles. This implies that these particles were formed in the period of the AZ31 sheet making process. In other words, the details of the Mg alloy manufacturing process play a primary role in determining the size and distribution of residual Al_8Mn_5 products. The microstructure of AZ31 alloy welds, therefore, will be influenced by the sheet metal manufacturing process.

According to the heat input during RSW of AZ31, the temperature of the welding zone can reach 650 to 770 °C.[31] This implies that spontaneous melting of second-phase Al_8Mn_5 particles is precluded since this intermetallic has a melting temperature of 1048 to 1191 °C,[28] which is much higher than the highest predicted temperature of the fusion zones. Therefore, these pre-existing Al_8Mn_5 particles in AZ31 alloys sheets will remain solid and can act as inoculants to promote the nucleation of new grains in the fusion zone.

B. *Effect of Second-Phase Particles on Columnar-to-Equiaxed Transition*

Different microstructures were observed across the RSW welds of AZ31 SA and SB alloys, which have a similar chemical composition but different sizes of second-phase particles. It is usually believed that solification morphology in any welds of given alloys is related to the ratio of G/R.[4,7,9,11] During RSW, weld pool solidification always starts from the parent metal partially molten zone with a minimum degree of undercooling since the solidification phase has the same crystalline structure with the BM. This leads to the well-known epitaxial growth without requiring any nucleation event. The columnar dendritic grains, which have their easy growth direction lining up favorably with the direction of maximum temperature gradient, tend to grow faster and crowd out other columnar grains.

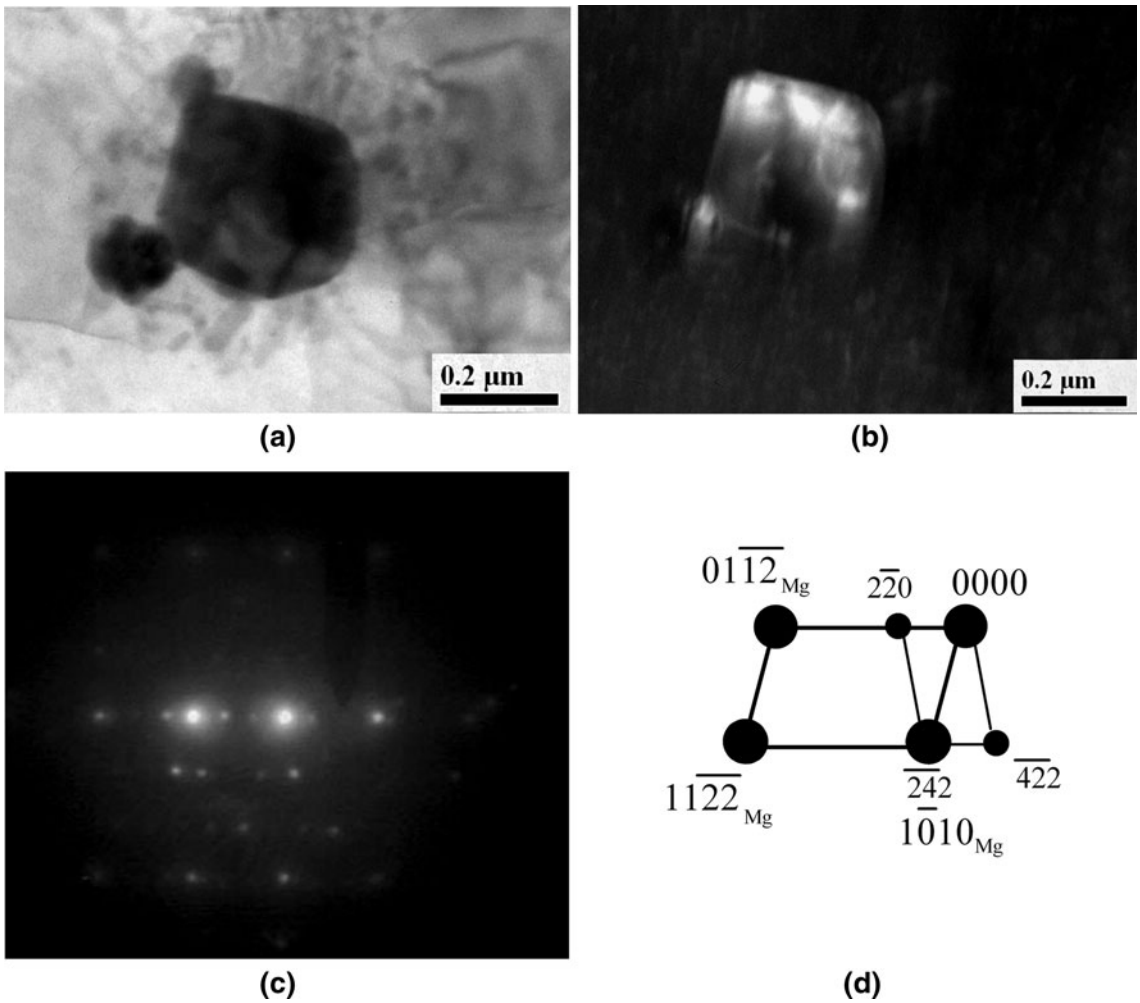

Fig. 11—TEM image, SADP, and EDS analysis of the Al-Mn-Zn particles in the SA alloy: (*a*) bright field, (*b*) dark field, (*c*) SADP, and (*d*) its schematic representation in $[24\bar{2}3]_{Mg}$ zone axis.

A columnar dendritic structure is produced, as shown in the SB alloy (Figures 3(b) and 4(b)).

If the size of second-phase particles in front of the interface is significantly less than the critical embryo radius, r^*, few new grains will nucleate in the molten pool under typical welding conditions. If the size is above the r^*, the nucleation of new grains is possible. However, when the size is not large enough, then any growing equiaxed grains will be trapped by the progressing columnar grains and the grown macrostructure will retain a columnar dendritic morphology (Figure 4(b)). However, new grains will nucleate and grow if the second-phase particles are large enough to become nuclei in the areas near the fusion boundary. These coarse second-phase particles block off the epitaxial columnar grains. Consequently, the main growth competition can switch from being among epitaxial columnar grains themselves to between epitaxial columnar grains and new grains formed in the fusion zone. Columnar dendritic grain growth will be restricted, and equiaxed grains will partially replace the columnar ones, as displayed in the AZ31 SA alloy welds (Figures 3(a) and 4(a)). Meanwhile, the grains could be refined in the central areas of AZ31-SA weld as the nucleation efficiency of the coarse nuclei increased (Figure 5(a)).

When nucleant particles are present in the molten pool, thermal and constitutional undercooling driven heterogeneous nucleation is believed to play an important role in promoting columnar-to-equiaxed transition. The heterogeneous nucleation would occur ahead of the columnar front once the undercooling suffices to induce heterogeneous nucleation, depending upon the inoculant sizes. The dependence of nucleation efficiency on the size and surface properties of the foreign nucleating particles was investigated by Fletcher.[32] It has been well accepted that the size effect of a nucleant particle is related to the critical embryo radius, r^*, which is a function of the undercooling. It was recently demonstrated that the larger the nucleant particles, the more effective they are, when the radius of the nucleant particle, R, is smaller than $5r^*$.[33] However, little further influence of the nucleant particle size on heterogeneous nucleation will be displayed, when $R > 5r^*$.[33]

According to Reference 33, the r^* for nucleation of Mg could be estimated with the following equation:

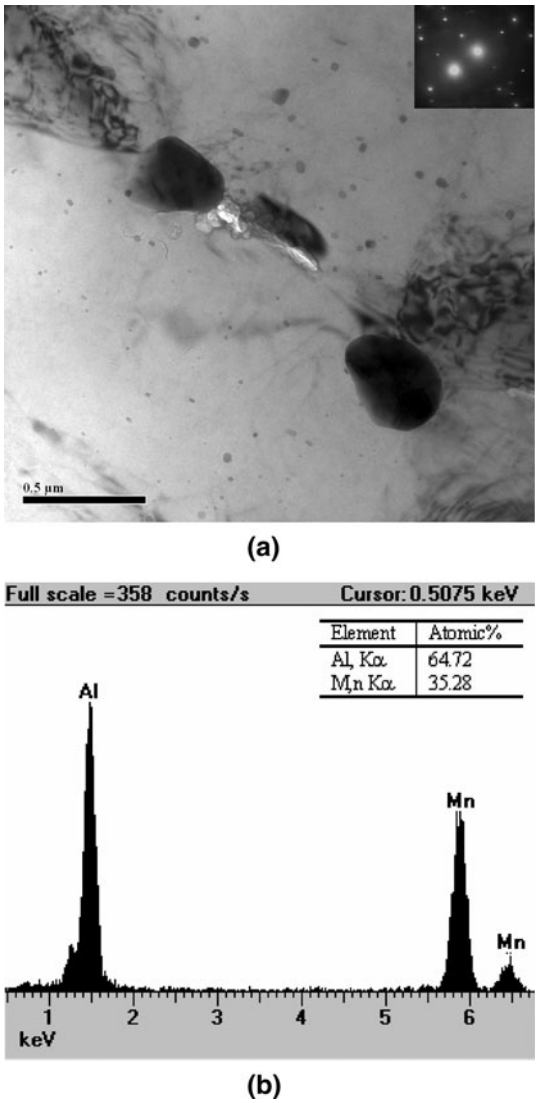

Fig. 12—TEM image and EDS analysis of the Al-Mn particles in the SB alloy: (*a*) TEM image and (*b*) EDS.

$$r* = -\frac{2\gamma_{SL}T_m}{L_V\Delta T} \quad [1]$$

where the melting point of Mg is $T_m = 923$ K, the solid/liquid interfacial free energy is $\gamma_{SL} = 0.115$ Jm^{-2}, and the latent heat of fusion per unit volume of solid Mg is $L_V = 5.989 \times 10^8$ Jm^{-3}. ΔT is the undercooling required to overcome the free-growth barrier for the effective initiation of a grain on particles. Therefore, the critical embryo radius in α-Mg can be estimated by the following equation:[34]

$$r* = 0.354/\Delta T \quad [2]$$

The critical embryo radius r^* is typically of the order of magnitude of 10^{-1} μm in many cases.[34] This means that the size effect will be observed by using substrate particles of less than 1 μm in diameter ($2R < 10\ r^*$). To enhance heterogeneous nucleation, the substrate radius needs to be at least 5 times that of the critical embryo radius. In other words, the coarser the Al_8Mn_5 particles, the more efficient the nucleation and the more grain refining of the weld, when the diameter of the nucleant is up to 1 μm. No extra promotion of nucleation would be observed when the diameter of the nucleant is larger than 1 μm. Therefore, the Al_8Mn_5 particles with 4 to 10 μm in the SA alloy welds can be expected to have higher efficiency of nucleation than those with 0.09 to 0.2 μm in the SB alloy welds.

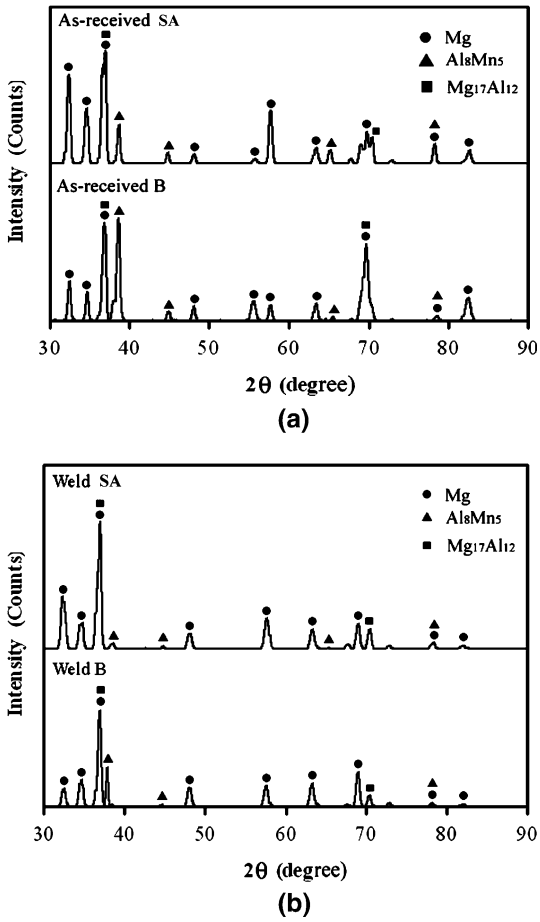

Fig. 13—XRD curves of the AZ31 alloys: (*a*) as-received condition and (*b*) welds.

C. *Columnar-to-Equiaxed Transition Induced by Adding Mn Particles into the SB Alloy*

In order to confirm the effects of second-phase particles on the microstructure formed in AZ31 Mg alloy, coarse Mn particles, ~10 μm in length, were intentionally added into the fusion zone of some AZ31 SB welds, which did not contain coarse Al_8Mn_5 particles in the as-received condition. Welds were doped with Mn by placing powders on the surface of the sheets in the welding areas before welding. All welding parameters were kept the same as the previous tests on the as-received SA and SB alloy sheets. Typical optical microstructure across the weld of the SB alloy specimen with added Mn particles is shown in Figure 14. This microstructure is similar to that formed in the SA alloy,

which contains the coarse Al_8Mn_5 particles. This result clearly demonstrated that the introduced Mn particles dramatically restricted the growth of columnar dendritic structure within an area of 420 μm in width and promoted the columnar-to-equiaxed transition in the AZ31 SB alloy welds. Furthermore, these microstructures formed in the SB alloy welds with added Mn particles were analyzed via SEM and EDS. Some equiaxed dendritic grains were observed to nucleate on the surface of the added Mn particles, as shown in Figure 15(a). This inoculant was determined by EDS to be Mn particles, as shown in Figure 15(b). This result confirms that the reduction of the columnar dendritic structure in the AZ31 alloy SA weld can be attributed to the pre-existence of coarse Al-Mn intermetallic second-phase particles in the AZ31 Mg alloy.

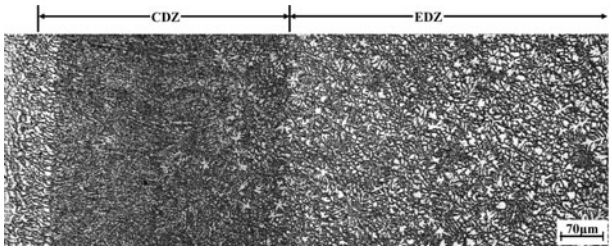

Fig. 14—Microstructure variation across RSW AZ31 SB alloy welds with addition of Mn particles.

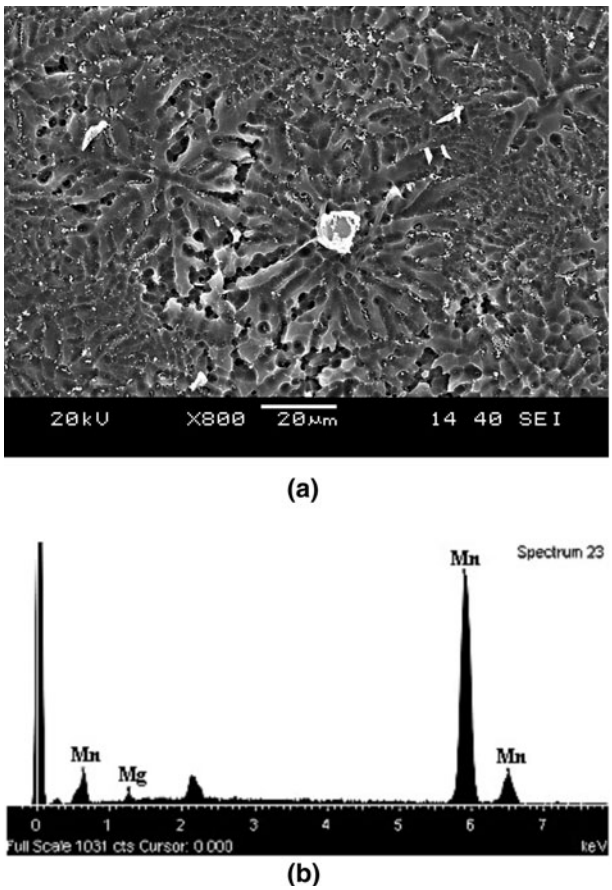

Fig. 15—Illustration of an added Mn particle as a nucleus of equiaxed dendritic grain: (*a*) SEM image and (*b*) EDS.

D. *Other Factors Affecting Columnar-to-Equiaxed Transition*

The columnar-to-equiaxed transition in AZ31 Mg alloy welds can be affected by several other factors such as welding heat input, cooling rate, and chemical compositions of BMs, besides the second-phase particles of relatively high melting temperature.

It is well known that the higher the cooling rate, the shorter the solidification time of welds, and the finer the dendritic structure becomes.[6] As the welding heat input increases, the temperature gradient (G) of the melt pool is reduced. This effect results in limiting constitutional supercooling and promoting equiaxed grains, which in turn block off the growth of columnar grains.[11] In this work and the examined welding conditions, the nugget size of two AZ31 Mg alloys is almost the same (Figures 2(a) and (b)). Therefore, it is believed that the welding heat input and cooling rate should be similar for the SA and SB alloy welds. However, different from the case of casting, the cooling rate is much faster during RSW. That leads to a high thermal undercooling of welds. Since the melting temperature of AZ31 Mg alloys is approximately 640 to 670 °C during welding in the present welding condition and the melting temperature of the ternary eutectic Mg-Al-Zn is about 430 °C,[28] the thermal supercooling temperature of AZ31 Mg alloy welds could be as high as ΔT = 210 to 240 °C.

Thermal undercooling is believed to play a significant role in promoting the columnar-to-equiaxed transition in AZ31 Mg alloy resistance spot welds. However, this thermal undercooling should not lead to an obvious difference of microstructure between the SA and SB alloys, since they have the similar heat input at the same welding condition. Therefore, it is believed that constitutional undercooling and second-phase particles play a predominant role in restricting the growth of columnar dendritic structure in the SA alloy and lead to a different microstructure between the SA and SB alloy welds. The details of effects of thermal undercooling on microstructure of AZ31 Mg alloy welds under different welding conditions will be reported in another article.[27]

For the effect of chemical compositions of BMs, solute atom zinc (Zn) may have an influence on the width of CDZ by promoting the formation of nuclei for equiaxed dendritic structure,[19] since Zn concentration in the SA alloy (1.09 pct) is higher than that in the SB alloy (0.8 pct). The equilibrium solid solubility of Zn in Mg substantially decreases with temperature. Zn is next to aluminum in effectiveness as an alloying ingredient to strengthen AZ 31 Mg alloy. The primary effect of the added Zn is believed to be the promotion of the age hardening effect of Mg-Al precipitates and improvement of the creep properties of AZ31 alloys.[35] On the other hand, Zn was observed to form fine precipitates of $MgZn_2$ compound of around 0.04 μm during double aging in ZM61 and ZMA611 Mg alloys.[36,37] Therefore, the higher concentration of Zn in the SA alloy could

form $MgZn_2$ with a size of 0.04 μm, which is similar in size to the submicron Al_8Mn_5 existing in both the SA and SB alloys. Therefore, the difference of Zn concentration should not make a large contribution to the microstructure refinement of AZ31 Mg alloy welds, compared to that of the much larger Al_8Mn_5 particles present only in the SA alloy.

V. SUMMARY AND CONCLUSIONS

1. The typical weld microstructure of AZ31 Mg alloys consists of four distinct regions: BM, HAZ, CDZ, and EDZ in the fusion zone. The primary microstructural difference between AZ31 SA and SB alloy welds was found to be the size of the CDZ. Columnar dendritic grains were well developed in the SB alloy welds, while they were restricted within a narrow region near the fusion boundary by an earlier transition from columnar to equiaxed structure in the SA alloy welds.
2. Even though the two AZ31 Mg alloys have similar chemical compositions, different manufacturing processes lead to the formation of different sizes of second-phase particles in the SA and SB alloys in the as-received condition. Coarse Al_8Mn_5 particles of 4 to 10 μm in length were only formed in the SA alloys. Submicron Al_8Mn_5 second-phase particles of 0.09 to 0.4 μm in length were observed to be present in both SA and SB alloys. All of these Al-Mn intermetallic particles were pre-existing from the sheet manufacturing process and were not apparently changed significantly by the transient melting during weld nugget formation.
3. The pre-existing Al_8Mn_5 intermetallic compound particles could act as nuclei of α-Mg nucleation during the solidification of the AZ31 Mg alloys in RSW. The refined microstructure in the vicinity of the fusion boundary in the SA alloy could be attributed to the pre-existing coarse second-phase particles of Al_8Mn_5, which play the role of inoculants causing heterogeneous nucleation on their surface during weld nugget solidification. The coarser the particles, the more efficient the nucleation of α-Mg was found to be.
4. Columnar dendritic grains can be restrained and equiaxed grains can be promoted by adding some coarse Mn particles of ~10 μm in length into the fusion zone of AZ31 SB alloy welds, which do not contain any coarse Al-Mn particles in the as-received condition.

ACKNOWLEDGMENTS

This research is financially supported by the Natural Sciences and Engineering Research Council (NSERC), Canada Magnesium Strategic Network, and AUTO 21 Network of Centres of Excellence of Canada.

REFERENCES

1. S.H. Wu, J.C. Huang, and Y.N. Wang: *Metall. Mater. Trans. A*, 2004, vol. 35A, pp. 2455–69.
2. L.M. Liu, Z.D. Zhang, G. Song, and L. Wang: *Metall. Mater. Trans. A*, 2007, vol. 38A, pp. 649–58.
3. D.G. McCartney: *Int. Mater. Rev.*, 1989, vol. 34, pp. 247–60.
4. S.A. David and J.M. Vitek: *Int. Mater. Rev.*, 1989, vol. 34, pp. 213–45.
5. W. Kurz and D.J. Fisher: *Fundamentals of Solidification*, Trans Tech SA, Aedermannsdorf, Switzerland, 1989, pp. 51–92.
6. S. Kou: *Welding Metallurgy,* 2nd ed., Wiley Interscience, John Wiley & Sons, Inc., Hoboken, NJ, 2003, pp. 199–214.
7. T. Ganaha, B.P. Pearce, and H.W. Kerr: *Metall. Trans. A*, 1980, vol. 11A, pp. 1351–59.
8. B.P. Pearce and H.W. Kerr: *Metall. Trans. B*, 1981, vol. 12B, pp. 479–86.
9. J.C. Villafuerte, E. Pardo, and H.W. Kerr: *Metall. Trans. A*, 1990, vol. 21A, pp. 2009–19.
10. S. Kou and Y. Le: *Weld J.*, 1986, vol. 65, pp. 305s–13s.
11. S. Kou and Y. Le: *Metall. Trans. A*, 1988, vol. 19A, pp. 1075–82.
12. F. Matsuda, H. Nakagawa, K. Nakata, and R. Ayani: *Trans. JWRI*, 1978, vol. 7, pp. 111–27.
13. G.D.J. Ram, T.K. Mitra, V. Shankar, and S. Sundaresan: *J. Mater. Process. Technol.*, 2003, vol. 142, pp. 174–81.
14. T. Koseki and G. Thewlis: *Mater. Sci. Technol.*, 2005, vol. 21, pp. 867–79.
15. P. Cao, M. Qian, and D.H. StJohn: *Scripta Mater.*, 2006, vol. 54, pp. 1853–58.
16. D. Qiu, M.X. Zhang, J.A. Taylor, H.M. Fu, and P.M. Kelly: *Acta Mater.*, 2007, vol. 55, pp. 1863–71.
17. T. Ganaha and H.W. Kerr: *Met. Technol.*, 1978, vol. 5, pp. 62–69.
18. D.L. Hallum and W.A. Baeslack, III: *Welding J.*, 1990, vol. 69, pp. 326s–336s.
19. M. Kato, F. Matsuda, and T. Senda: *Trans. Jpn. Welding Soc.*, 1972, vol. 3, pp. 69–76.
20. N. Tiner: *AIME Tech. Pub.*, 1945, vol. 12, pp. 1–12.
21. J.Y. Byun, S. Kwon, H.P. Ha, and J.K. Yoon: in *Magnesium Alloys and Their Applications*, K.U. Kainer, ed., Wiley-VCH, Weinheim, 2003, p. 713.
22. T. Laser, M.R. Nurnberg, A. Janz, Ch. Hartig, D. Letzig, R. Schmid-Fetzer, and R. Bormann: *Acta Mater.*, 2006, vol. 54, pp. 3033–41.
23. Y. Tamura, J. Yagi, T. Haitani, N. Kono, and H. Tamehiro: *Mater. Trans.*, 2003, vol. 44, pp. 552–57.
24. D.Q. Sun, B. Lang, D.X. Sun, and J.B. Li: *Mater. Sci. Eng. A*, 2007, vols. 460–461, pp. 494–98.
25. L. Yu, K. Nakata, N. Yamamoto, and J. Liao: *Mater. Lett.*, 2009, vol. 63, pp. 870–72.
26. L. Liu, S. Zhou, Y. Tian, J. Feng, J. Jung, and Y. Zhou: *Sci. Technol. Welding Joining*, 2009, vol. 14, pp. 356–61.
27. L. Liu, L. Xiao, J.C. Feng, Y.H. Tian, S.Q. Zhou, and Y. Zhou: unpublished research, 2010.
28. M. Ohno and R. Schmid-Fetzer: *Z Metallkd.*, 2005, vol. 96, pp. 857–69.
29. T. Laser, C. Hartig, M.R. Nurnberg, D. Letzig, and R. Bormann: *Acta Mater.*, 2008, vol. 56, pp. 2791–98.
30. C. Liu, F. Pan, and W. Wang: *Mater. Sci. Forum,* 2007, vols. 546–549, Part 1, pp. 395–98.
31. J.C. Feng, Y.R. Wang, and Z.D. Zhang: *Sci. Technol. Welding Joining*, 2006, vol. 11, pp. 154–62.
32. N.H. Fletcher: *J. Chem. Phy.*, 1958, vol. 29, pp. 572–76.
33. M. Qian and J. Ma: *J. Chem. Phys.*, 2009, vol. 130, pp. 214709-1–214709-7.
34. M. Qian and A. Das: *Scripta Mater.*, 2006, vol. 54, pp. 881–86.
35. J. Buha: *Mater. Sci. Eng. A*, 2008, vol. 492, pp. 11–19.
36. S.S. Park, G.T. Bae, D.H. Kang, I.H. Jung, K.S. Shin, and N.J. Kim: *Scripta Mater.*, 2007, vol. 57, pp. 793–96.
37. S.S. Park, Y.S. Oh, D.H. Kang, and N.J. Kim: *Mater. Sci. Eng. A*, 2007, vols. 449–451, pp. 352–55.